JOURNAL OF MAGNETIC RESONANCE, Series B **113,** 179–183 (1996)
ARTICLE NO. 0173

COMMUNICATIONS

Gradient-Echo Imaging Considerations for Hyperpolarized ^{129}Xe MR

LEI ZHAO,*,† ROBERT MULKERN,‡ CHING-HUA TSENG,*,§ DANIEL WILLIAMSON,* SAMUEL PATZ,* ROBERT KRAFT,* RONALD L. WALSWORTH,§ FERENC A. JOLESZ,* AND MITCHELL S. ALBERT*,¶

**Department of Radiology, Brigham and Women's Hospital and Harvard Medical School, Boston, Massachusetts 02115; †Department of Biomedical Engineering, Boston University, Boston, Massachusetts 02215; ‡Department of Radiology, Children's Hospital and Harvard Medical School, Boston, Massachusetts 02115; and §Harvard–Smithsonian Center for Astrophysics, Cambridge, Massachusetts 02138*

Received August 19, 1996

Magnetic-resonance imaging using the novel MR signal source provided by hyperpolarized noble gases ^{129}Xe and ^{3}He may prove to be an important new diagnostic technique for medical imaging (*1*). Imaging with a hyperpolarized noble gas is different in many ways from conventional imaging. The large nonequilibrium polarization of the nuclei is nonrenewable; hence, special considerations are required when designing suitable imaging pulse sequences. Every excitation pulse destroys some of the hyperpolarized longitudinal magnetization, which then cannot be restored by waiting for relaxation back to thermal equilibrium as in conventional MRI. This disadvantage is offset by the elimination of long recycle delays. In particular, high-speed gradient-echo techniques can be developed that are especially suitable for imaging hyperpolarized noble gases.

In this Communication, we investigate gradient-echo imaging strategies for hyperpolarized ^{129}Xe MRI. We find that the choice of flip angle, sampling order, and resolution has critical consequences for image quality. Sobering *et al.* recently suggested a variable-flip-angle approach for hyperpolarized ^{129}Xe (*2*), and several authors have previously applied this technique to conventional MRI using thermally polarized protons (*3–5*). Here we report experiments on the use of different gradient-echo pulse sequences and find that a variable-flip-angle approach can improve the hyperpolarized ^{129}Xe signal-to-noise ratio (SNR) and eliminate some typical image artifacts. We also demonstrate that, although a constant signal intensity can be obtained with such an approach, the maximum spatial resolution achievable is constrained by the longitudinal relaxation time, T_1, of the hyperpolarized ^{129}Xe.

Hyperpolarization of ^{129}Xe is achieved by collisional spin exchange with optically pumped rubidium vapor, which yields up to 100,000-fold enhancement in spin polarization and MR detectability (*6*). We used natural abundance xenon (26% ^{129}Xe), which was contained in a 25 cm^3 cylindrical glass cell (2 cm diameter, 7.5 cm length), at 3 atm, along with 3 atm N_2 buffer gas and a small quantity of solid Rb. ^{129}Xe was hyperpolarized in the fringe field of a 1.5 T superconducting magnet. Circularly polarized 795 nm light from diode laser arrays (Optopower, Tucson, Arizona) was used for optical pumping of the Rb vapor. After 30 min of optical pumping at 90–100°C, the glass cell was rapidly cooled in ice water to remove the Rb vapor by condensation onto the cell walls. ^{129}Xe spectra and images were obtained at 17.7 MHz on a 1.5 T magnet interfaced with a SMIS spectroscopy/imaging system. Spoiler gradients were used in all experiments to dephase residual transverse magnetization remaining after each acquisition. This was required because of the long T_2^* values of ^{129}Xe in the gas phase.

Several investigators have used low-flip-angle gradient-echo techniques such as fast low-angle shot (FLASH) (*7*) for imaging hyperpolarized ^{129}Xe and ^{3}He (*1, 8–12*). The use of repeated small-flip-angle excitation pulses is especially suitable for imaging hyperpolarized species in experiments involving the administration of an initial bolus of hyperpolarized gas. Since repetitive sampling of the residual longitudinal magnetization causes nonrenewable depletion, low-flip-angle excitations are effective in preserving the polarization while all rows of *k* space are sampled. The longitudinal magnetization remaining after *n* excitation pulses is proportional to $(\cos\theta)^n$, where θ is the pulse flip angle. Using too small a flip angle, however, results in unacceptably low SNR.

Let us consider a system of hyperpolarized spins with longitudinal magnetization αm_{00}, where m_{00} is the thermal equilibrium longitudinal magnetization enhanced by the hyperpolarization factor α. The FID amplitude for the nth excitation pulse is given by $\alpha m_{00}\cos^{n-1}\theta \sin\theta$, ignoring T_1 relaxation. This relationship is demonstrated in Fig. 1a, which shows observed hyperpolarized ^{129}Xe signal amplitudes of the xenon pumping cell for a train of 128 12° pulses (filled

¶ To whom correspondence should be addressed.

1064-1866/96 $18.00

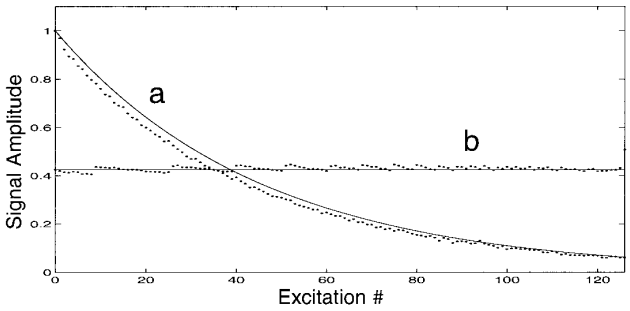

FIG. 1. (a) Hyperpolarized ^{129}Xe signal amplitude for a train of 12° pulses. The filled circles represent experimental data. The solid line is the theoretical signal amplitude expected. (b) Hyperpolarized ^{129}Xe signal obtained using a variable-flip-angle pulse sequence. Filled circles represent experimental data; the straight line is the theoretical signal amplitude. The slight rise and fall of the signal is due to the inability of the spectrometer to generate flip-angle increments smaller than 0.1°. The initial flip angle was 5.07° and the last was 90°.

circles). Because the T_1 value of the xenon cell was long, about two hours, compared with the TR value of 100 ms, the experimental results are in close agreement with the theoretically expected signal amplitude, in which T_1 relaxation was ignored (Fig. 1a, solid line).

A disadvantage encountered using conventional constant-flip-angle sequences for imaging of hyperpolarized species is the progressively diminishing signal strength during the course of acquisition: since a fraction of the longitudinal magnetization is depleted after each excitation pulse, a constant-flip-angle sequence generates a steadily decreasing signal for acquisition of each subsequent line in k space. The effect of this nonlinear sampling is to introduce an artifact along the phase direction of the image (*4, 13–15*). Centrically ordered phase encoding results in a loss of high-frequency spatial information, whereas sequential encoding underrepresents the center of k space, causing a loss in overall SNR, and unequal representation of the high spatial frequencies. To correct for this decreasing SNR, the pulse flip angle can be progressively increased during the course of acquisition (*2–5*). Employing a variable-flip-angle scheme to maintain a constant transverse magnetization, the flip angle, θ_n, for the nth excitation pulse, ignoring T_1 relaxation, is given by

$$\theta_n = \tan^{-1}\left(\frac{1}{\sqrt{N-n}}\right), \qquad [1]$$

where N is the total number of excitation pulses. Note that the last flip angle generated by this algorithm will correspond to a 90° pulse, effectively using all of the remaining magnetization.

Figure 1b shows a plot of the hyperpolarized ^{129}Xe signal amplitude employing the variable-flip-angle technique (data, filled circles; theoretical, solid line). Note the constant signal amplitude response over the course of the acquisition train. (The slight rise and fall of the signal is due to the inability of the spectrometer to generate flip-angle increments smaller than 0.1° in this case.) A 90° pulse applied to the sample following this experiment produced no significant signal, evidence that the variable-flip-angle sequence effectively utilized all of the available magnetization.

An interesting feature of hyperpolarized noble gas MR is that the longitudinal relaxation times, T_1, are typically quite long (*16*); for example, we observed up to three hours for xenon as a pure gas at 1.5 T. In biological tissues *in vivo*, the T_1 values for ^{129}Xe decrease to the 1 to 100 seconds range (*11, 17*), ensuring that longitudinal relaxation will play a role in imaging xenon in biological tissues with gradient-echo sequences lasting some 500 ms or more.

Let us now consider the effects of relaxation. Consider a gradient-echo sequence of the form θ_1—TR—θ_2—TR—$\cdots\theta_N$ with a total of N pulses with variable flip angle θ_j and with the phases of the RF pulses all along the x axis of the rotating frame. To determine the signal available after each pulse, a Bloch equation analysis is performed with two assumptions. The first assumption is that complete spoiling of the transverse magnetization is achieved prior to each RF pulse. This may be accomplished with spoiling gradients or may occur naturally given relatively fast T_2^* transverse relaxation and sufficiently long TR periods. The second assumption is that the thermal equilibrium term, $m_{00}[1-\exp(-\mathrm{TR}/T_1)]$, which should be added to the longitudinal relaxation at the end of each TR period, is negligible. This is tantamount to ignoring all terms in the longitudinal magnetization Bloch equation which are not proportional to the hyperpolarization constant α and is justified by the large values of α, typically 10,000 or more, experimentally attainable for both ^{129}Xe and ^{3}He (*1, 8, 18*). Such large hyperpolarization factors make tracking the conventional thermal equilibrium magnetization relevant only once the hyperpolarized state has diminished to levels approaching thermal equilibrium. At this point, the signal levels are too small to use in single-shot imaging sequences. Thus the approximation assumes that we are only considering images generated from signals well above thermal equilibrium. Given these assumptions, a Bloch equation analysis yields the transverse magnetization following the nth RF pulse to be

$$S_n = \alpha m_{00}\exp[-(n-1)\mathrm{TR}/T_1]\sin\theta_n\prod_{j=1}^{n-1}\cos\theta_j. \qquad [2]$$

For a constant flip angle θ, the trigonometric term becomes simply $\sin\theta\cos^{(n-1)}\theta$. The more general form given in Eq. [2] allows us to examine the effects of variable flip angles during the course of the sequence. In particular, from Eq. [2] a recursive relation is derived for incrementing the flip

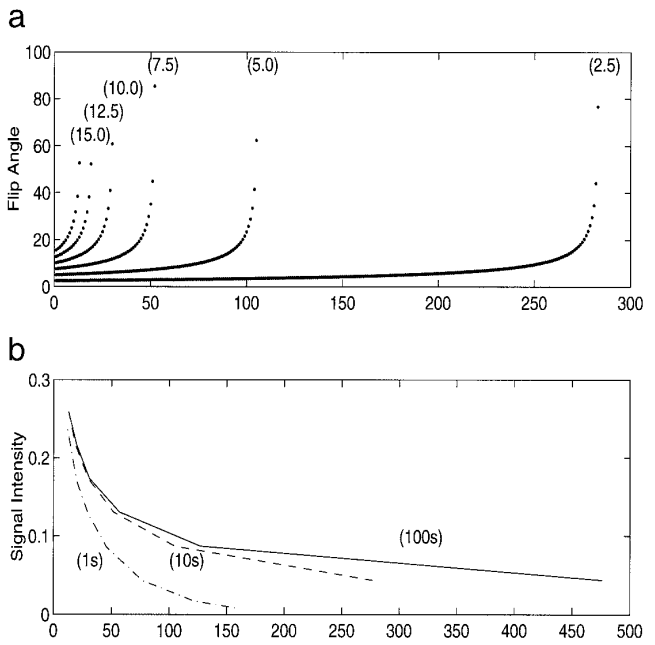

FIG. 2. (a) Simulation demonstrating the relationship of the initial flip angle and total number of pulses that can be applied to achieve a constant signal using a variable-flip-angle sequence assuming a T_1 of 10 s and TR of 20 ms. The recursively calculated flip angle is plotted as a function of pulse number for five different initial flip angles ranging from 2.5° to 15° in steps of 2.5°. (b) Demonstration of the relation between maximum signal intensity and number of phase-encoding steps accessible with the recursively incremented-flip-angle approach for T_1 values of 1, 10, and 100 s, using a TR of 20 ms.

angle such that the signal remains constant at its initial level of $S_1 = \alpha m_{00} \sin \theta_1$. To ensure this constancy of signal, we must let the nth flip angle be

$$\theta_n = \sin^{-1}\left[\frac{\exp[(n-1)\mathrm{TR}/T_1]\sin\theta_1}{\prod_{j=1}^{n-1}\cos\theta_j}\right]. \qquad [3]$$

The flip angle can be incremented according to Eq. [3] until θ reaches $\pi/2$, at which point the magnetization will be exhausted. Thus, depending on the T_1 value, the initial flip angle, and the TR value, the number of pulses which can be applied is limited as is the total number of phase-encoding steps available. Figure 2a demonstrates this effect for the case of $T_1 = 10$ s and a TR value of 20 ms. The recursively calculated flip angle is plotted as a function of pulse number for five different initial flip angles from 2.5° to 15°, in steps of 2.5°. As may be seen, the smaller the flip angle, the larger the number of pulses or, equivalently, phase-encoding steps. Note that even with a flip angle as low as 5°, the standard use of 128 phase-encoding steps is prohibited with the recursively incremented-flip-angle approach for this T_1 value. In general, signal must be sacrificed to increase the number of available phase-encoding steps. Equation 3 may be used to study the relationship between signal intensity, T_1, and number of phase encode steps. Figure 2b demonstrates this relationship with the recursively incremented-flip-angle approach for T_1 values of 1, 10, and 100 s. This is the relevant range recently associated with biological tissue ^{129}Xe T_1 values (*11, 17, 19*). Note that if $\mathrm{TR}/T_1 \ll 1$, then Eq. [3] reduces to Eq. [1] and the effects of longitudinal relaxation can be ignored.

We have modeled both the variable-flip-angle (VFA) and constant-flip-angle (CFA) sequences, using phase profiles along the length of a hyperpolarized ^{129}Xe gas cell (rectangular profile), to point out the relative advantages of the VFA approach. The left panel of Fig. 3 shows the simulated profiles along the phase direction for the cases of sequential CFA (Fig. 3a), centric CFA (Fig. 3b), and sequential VFA (Fig. 3c) using 128 phase-encoding steps. While a substantial ringing artifact is present in the sequential CFA simulation (Fig. 3a), and an edge-blurring artifact in the centric CFA profile (Fig. 3b), the VFA profile (Fig. 3c) more accurately represents the original object. With maintenance of the echo amplitude by the use of VFA, the *k*-space trajectory becomes irrelevant. Figures 3d–3f display the experimental phase profiles obtained using the above three approaches. The experimental profiles resemble the simulations. We attribute the rise near the edges of the profiles to a combination of two effects. First, the gas cell contains two tips, created by flame sealing during the filling process giving more gas volume in these regions. Since no slice selection was used during excitation, the phase profiles include these regions of excess gas near the ends of the cell due to volume averaging.

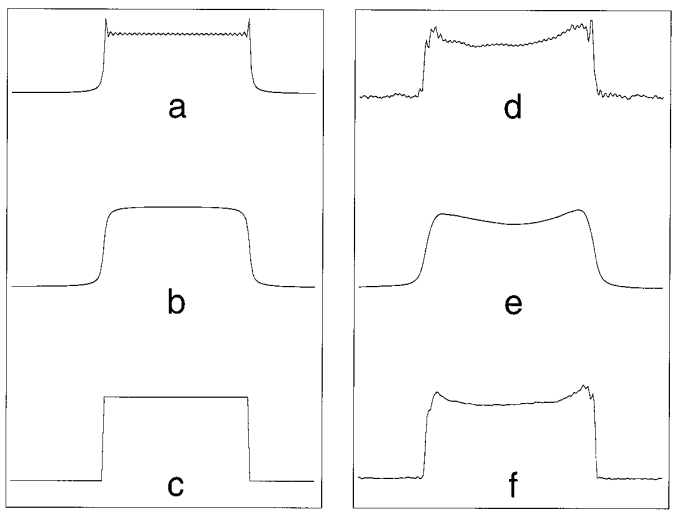

FIG. 3. (Left) Simulated profiles of the xenon pumping cell along the phase direction (rectangular profile) for the cases of (a) sequential CFA, (b) centric CFA, and (c) sequential VFA using 128 phase-encoding steps. (Right) Experimental phase profiles obtained using (d) sequential CFA, (e) centric CFA, and (f) sequential VFA. For both the simulations and the experiments, 128 phase-encoding steps were employed. (a), (b), and (c) are not normalized to each other, but scaled to best demonstrate the artifacts.

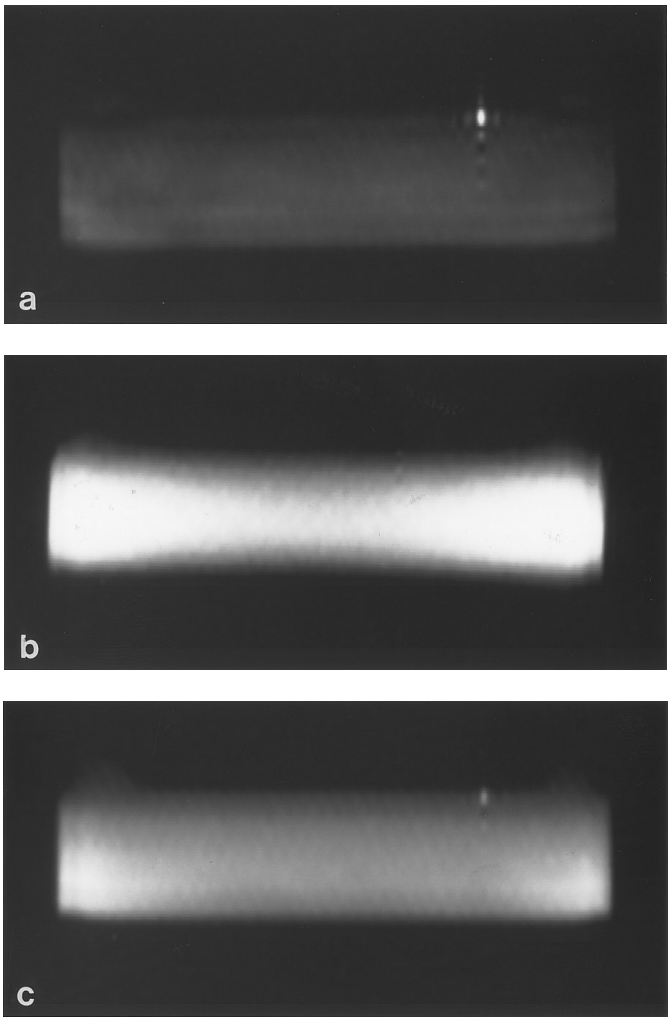

FIG. 4. Hyperpolarized ^{129}Xe gradient-echo images obtained using (a) sequentially ordered CFA, (b) centrically ordered CFA, and (c) sequentially ordered VFA sequences. The images were obtained on sequential runs using the same hyperpolarized pumping cell with the same initial polarization. All images were processed using the same gray-scale window and contrast level.

Second, the large diffusion constant for xenon (*20*) may cause restricted diffusion at the end of the cell due to reflection of the spins at the edge boundaries (*21, 22*). A quantitative investigation of the effect of diffusion on imaging hyperpolarized ^{129}Xe will be the subject of future work.

Hyperpolarized ^{129}Xe images of a cylindrical gas cell are shown in Fig. 4. Figure 4a was obtained using sequentially phase-ordered CFA. Figure 4b shows the result using centrically ordered CFA. Figure 4c is the image obtained using sequentially ordered VFA. The images were obtained on successive runs using the same hyperpolarized pumping cell with the same initial polarization. All images were processed using the same gray-scale window and contrast level. Note the low SNR in the sequential CFA image (Fig. 4a) and the significant blurring of the horizontal edges of the concentric CFA image (Fig. 4b). The improved SNR and absence of phase artifact of the VFA image closely agree with the simulated results (Fig. 3). The ringing artifact is not seen along the phase direction of the sequential CFA image (Fig. 4a), although it is present in the simulation (Fig. 3a), because the axial profile of the cell is round instead of square. The much smaller signal that is encoded at the high-spatial-frequency components of k space for a round profile removes the ringing artifacts; however, shape distortions still remain.

In conclusion, substantial improvements in SNR and image quality can be obtained using VFA approaches. There is a trade-off between the maximum spatial resolution achievable and signal intensity using the VFA approach, which is constrained by the longitudinal relaxation time (T_1) of the hyperpolarized ^{129}Xe. We have experimentally demonstrated the improvement in image quality obtainable using a VFA sequence. Due to the typically long T_2 and T_2^* values of ^{129}Xe, further SNR improvements may be possible by employing multiple-echo-summation techniques. One could also consider the use of multiple echoes in echo-planar-imaging (EPI) formats in which the phase-encode steps are incremented from echo to echo to complete k-space sampling rapidly. Examples include the RARE and GRASE sequences, which are potential candidates for imaging hyperpolarized species (*23–25*). Such strategies will be explored in detail in a forthcoming paper. The specific gradient-echo sampling considerations described in this Communication are readily extendable to imaging hyperpolarized ^{3}He.

ACKNOWLEDGMENTS

This work was supported by the Whitaker Foundation (M.S.A., R.L.W.), the Air Force Office of Scientific Research, the George W. Burch Foundation, NASA, the Smithsonian Institution (R.L.W., C.H.T.), and NIH (C.H.T.). We thank Dilip Balamore and Dr. Koichi Oshio for stimulating discussions, and Daniel Kacher, Glenn Wong, and Dr. Eduardo Oteiza for technical assistance.

REFERENCES

1. M. Albert, G. Cates, B. Driehuys, W. Happer, B. Saam, C. S. Springer, and A. Wishnia, *Nature* **370,** 199 (1994).
2. G. S. Sobering and Y. Shiferaw, Abstracts of the Society of Magnetic Resonance, 3rd Annual Meeting, p. 979, 1995.
3. M. K. Stehling, *Magn. Reson. Imaging* **10,** 165 (1992).
4. J. P. Mugler III, F. H. Epstein, and J. R. Brookeman, *Magn. Reson. Med.* **28,** 165 (1992).
5. S. J. Wang, D. G. Nishimura, and A. Macovski, *Magn. Reson. Med.* **17,** 244 (1991).
6. W. Happer, E. Miron, S. Schaefer, D. Schreiber, W. A. van Wijngaarden, and X. Zeng, *Phys. Rev. A* **29,** 3092 (1984).
7. A. Haase, J. Frahm, D. Matthaie, W. Haenicke, and K. D. Merboldt, *J. Magn. Reson.* **67,** 258 (1986).
8. H. Middleton, R. D. Black, B. Saam, G. D. Cates, G. P. Cofer, R. Guenther, W. Happer, L. W. Hedlund, G. A. Johnson, K. Juvan, and J. Swartz, *Magn. Reson. Med.* **33,** 271 (1995).

9. R. D. Black, H. L. Middleton, G. D. Cates, G. P. Cofer, B. Driehuys, W. Happer, L. W. Hedlund, G. A. Johnson, M. D. Shattuck, and J. C. Swartz, *Radiology* **199,** 867 (1996).
10. J. R. Macfall, H. C. Charles, R. D. Black, H. Middleton, J. Swartz, B. Saam, B. Driehuys, C. Erickson, W. Happer, G. Cates, G. A. Johnson, and C. E. Ravin, *Radiology* **200,** 553 (1996).
11. M. E. Wagshul, T. M. Button, H. F. Li, Z. Liang, C. S. Springer, K. Zhong, and A. Wishnia, *Magn. Reson. Med.* **36,** 183 (1996).
12. P. Bachert, L. R. Schad, M. Bock, M. V. Knopp, M. Ebert, T. Grossmann, W. Heil, D. Hofmann, R. Surkau, and E. W. Otten, *Magn. Reson. Med.* **36,** 192 (1996).
13. X. Zhou, Z. P. Liang, G. P. Cofer, C. F. Beaulieu, S. A. Suddarth, and G. A. Johnson, *J. Magn. Reson. Imaging* **3,** 803 (1993).
14. R. V. Mulkern, P. S. Melki, P. Jakab, N. Higuchi, and F. A. Jolesz, *Med. Phys.* **18,** 1032 (1991).
15. R. V. Mulkern, S. T. S. Wong, C. Winalski, and F. A. Jolesz, *Magn. Reson. Imaging* **8,** 557 (1990).
16. M. Gatzke, G. D. Cates, B. Driehuys, D. Fox, W. Happer, and B. Saam, *Phys. Rev. Lett.* **70,** 690 (1993).
17. K. Sakai, A. M. Bilek, E. Oteiza, R. L. Walsworth, D. Balamore, F. A. Jolesz, and M. S. Albert, *J. Magn. Reson. B* **111,** 300 (1996).
18. D. Raftery, H. Long, T. Meersmann, P. J. Grandinetti, L. Reven, and A. Pines, *Phys. Rev. Lett.* **66,** 584 (1991).
19. S. D. Swanson, M. S. Rosen, K. P. Coulter, R. C. Welsh, and T. E. Chupp, Abstracts of the Society of Magnetic Resonance, 4th Annual Meeting, p. 1360, 1966.
20. K. C. Hasson, G. D. Cates, K. Lerman, P. Bogorad, and W. Happer, *Phys. Rev. A* **41,** 3672 (1990).
21. B. Putz, D. Barsky, and K. Schulten, *Chem. Phys.* **183,** 391 (1991).
22. W. Happer and B. Saam, personal communication.
23. P. Mansfield and A. A. Maudsley, *J. Magn. Reson.* **27,** 101 (1977).
24. J. Hennig, A. Nauerth, and H. Friedburg, *Magn. Reson. Med.* **3,** 823 (1986).
25. K. Oshio and D. A. Feinberg, *Magn. Reson. Med.* **20,** 344 (1991).